



This is a repository copy of *Interfacial width and phase equilibrium in polymer-fullerene thin-films*.

White Rose Research Online URL for this paper:

<https://eprints.whiterose.ac.uk/152240/>

Version: Published Version

Article:

Hynes, E.L., Cabral, J.T., Parnell, A.J. orcid.org/0000-0001-8606-8644 et al. (5 more authors) (2019) Interfacial width and phase equilibrium in polymer-fullerene thin-films. *Communications Physics*, 2 (1). 112.

<https://doi.org/10.1038/s42005-019-0211-z>

Reuse

This article is distributed under the terms of the Creative Commons Attribution (CC BY) licence. This licence allows you to distribute, remix, tweak, and build upon the work, even commercially, as long as you credit the authors for the original work. More information and the full terms of the licence here:

<https://creativecommons.org/licenses/>

Takedown

If you consider content in White Rose Research Online to be in breach of UK law, please notify us by emailing eprints@whiterose.ac.uk including the URL of the record and the reason for the withdrawal request.



eprints@whiterose.ac.uk
<https://eprints.whiterose.ac.uk/>










COMMUNICATIONS PHYSICS

ARTICLE

<https://doi.org/10.1038/s42005-019-0211-z>

OPEN

Interfacial width and phase equilibrium in polymer-fullerene thin-films

E.L. Hynes ¹, J.T. Cabral ², A.J. Parnell ³, P. Gutfreund ⁴, R.J.L. Welbourn ⁵, A.D.F. Dunbar ⁶,
D. Môn¹ & A.M. Higgins ¹

Domain composition and interfacial structure are critical factors in organic photovoltaic performance. Here, we report neutron reflectivity, grazing-incidence X-ray diffraction and atomic force microscopy measurements of polymer/fullerene thin-films to test a hypothesis that these partially miscible blends rapidly develop composition profiles consisting of co-existing phases in liquid-liquid equilibrium. We study a range of polymer molecular weights between 2 and 300 kg mol⁻¹, annealing temperatures between 120 and 170 °C, and time-scales up to 10 min, yielding over 50 distinct measurement conditions. Model bilayers of fullerene-derivatives and polystyrene enable a rigorous examination of theoretical predictions of the effect of polymer mass and interaction parameter on the compositions, ϕ , and interfacial width, w , of the coexistent phases. We independently measure ϕ and w and find that both Flory-Huggins mean-field-theory and key aspects of self-consistent-field-theory are remarkably consistent with experiment. Our findings pave the way for predictive composition and interface design in organic photovoltaics based on simple experimental measurements and equilibrium thermodynamic theory.

¹ College of Engineering, Swansea University, Bay Campus, Fabian Way, Swansea, SA1 8EN Wales, United Kingdom. ² Department of Chemical Engineering, Imperial College London, London SW7 2AZ, United Kingdom. ³ Department of Physics and Astronomy, The University of Sheffield, Sheffield S3 7RH, United Kingdom. ⁴ Institut Laue-Langevin, 71 avenue des Martyrs, 38000 Grenoble, France. ⁵ ISIS Pulsed Neutron and Muon Source, Science and Technology Facilities Council, Rutherford Appleton Laboratory, Harwell Science and Innovation Campus, Didcot OX11 0QX, United Kingdom. ⁶ Department of Chemical and Biological Engineering, The University of Sheffield, Sir Robert Hadfield Building, Mappin Street, Sheffield S1 3JD, United Kingdom. Correspondence and requests for materials should be addressed to A.H. (email: a.m.higgins@swansea.ac.uk)

Solution-processed organic photovoltaics (OPVs) can now achieve power-conversion efficiencies of between 12% and 14% in binary^{1–8} and ternary⁹ blend devices, and 17% in tandem solar cells¹⁰. Over 10% efficiency was also recently reported for binary devices made by scalable processing methods in air⁸. This represents a significant rise in OPV performance over the last two decades that has resulted from the continued development of new materials³, and from optimisation strategies involving direct characterisation of the structure and properties of working devices¹¹. Significant effort has been dedicated to the characterisation of the morphology and domain composition within bulk heterojunctions^{11,12}, which are both key factors in relation to charge generation and transport^{13–16}. Fundamental studies focussed on understanding miscibility have also been performed by examining mixing within simplified bilayer architectures, particularly in fullerene/conjugated-polymer systems^{17–22}.

Owing to the tunable molecular weight (Mw) of polymers, mixing behaviour and hence film morphology can, in principle, be controlled independently of material chemistry. Phase separation in liquid mixtures²³, and morphology/performance in all-polymer²⁴ and polymer/small-molecule devices²⁵, can be strongly influenced by polymer size. However, the overall effects remain unclear; for instance, some OPV studies show a non-monotonic dependence of efficiency on Mw^{24–26}, whereas other closely related systems show no dependence at all²⁵. These results are variously rationalised in terms of domain-purity, domain-size, percolation pathways, preferential interfacial enrichment of components and crystallisation. However, characterisation and performance measurements of working devices alone are necessary but not sufficient for providing full understanding of these structurally complex blends (made from a wide-range of different material systems). The typically broad mass distributions in conjugated polymers has also resulted in the precise effects of Mw remaining elusive; polydispersity can affect both the thermodynamics^{27,28} and the (phase separation) kinetics of mixtures²⁹, but the most significant impact may be at interfaces where preferential segregation of lower mass polymer fractions (and hence the accumulation of chain ends) is possible^{30,31}.

Ye et al.³² recently studied mixing in bilayer systems and uncovered a striking correlation between device performance and fundamental parameters characterising the miscibility in polymer/small-molecule systems. Flory-Huggins theory was employed to interpret domain compositions and quantitatively link the interaction parameter, χ^{23} , to the device fill-factor, for an amorphous-polymer/fullerene and a range of polymer/small-molecule devices. Of key significance here, for a wide range of amorphous and semi-crystalline polymers, is the existence of mixed amorphous polymer/small-molecule phases^{17,19,22,33,34}, whose composition plays an important role in charge transport and charge recombination^{7,34}. The addition of mixed polymer/fullerene electron-transport layers can also significantly increase the efficiency and stability of perovskite solar cells³⁵. In both amorphous and semi-crystalline polymer systems, Ye et al. found that OPV device properties were controlled by the amorphous miscibility of the system. In addition to these findings, it is known that the composition of mixed amorphous domains within OPVs can result from the quenching of kinetic processes during fabrication as the system vitrifies on solvent evaporation, leading to non-equilibrium domain compositions within the (solvent-free) device. Given sufficient mobility (eg; potentially at the elevated temperatures reached in operation, or even at room temperature) such domains can change composition as they evolve towards equilibrium^{13,34,36}. This means that if domain compositions are optimised in the kinetically quenched state, failure of the system to remain fully vitrified will result in poor device stability^{13,34}. In

summary it is therefore clear that, in addition to the development of predictive capabilities for amorphous semiconducting polymer systems themselves (utilised in high efficiency³⁷ and high stability^{34,37} devices), the quantification of amorphous phase-behaviour is also required for a full understanding of efficiency and morphological stability in semi-crystalline-polymer/small-molecule devices.

In this work, we experimentally examine if and how polymer dimensions (Mw) can be employed to precisely determine equilibrium composition and interfacial width between coexisting polymer/fullerene (mixed) phases and establish the theoretical framework that enables their predictive design. We employ a thin-film bilayer annealing approach³⁸ that allows partially miscible systems to evolve to their equilibrium composition and thus determine the phase behaviour of the mixtures. Neutron reflectivity is used to measure composition profiles, as the high-resolution of this technique^{21,39} allows us to probe both the layer compositions, ϕ , and the interfacial width between phases, w , in the same samples, enabling comparison of our results with theoretical predictions for both ϕ and w , as a function of Mw. Atactic polystyrene (PS) is chosen as a well-understood model amorphous polymer, that can be synthesised across a wide mass range with control of Mw-distribution that is vastly superior to conjugated polymers; polydispersity indices in the present study are 1.05 or lower, in comparison to 1.3–1.8 in a recent study²⁵ or larger than 2 for many conjugated polymers³². This control is key in enabling high-resolution Mw studies (given the predicted dependence on Mw of both layer compositions and interface width, and the potential segregation of lower Mw fractions to surfaces/interfaces). We investigate thin-film geometries, where the sample thicknesses are of the same order as those used in the active layer of working devices (~100 nm). Such PS/fullerene bilayer systems offer good layer contrast and well-resolved reflectivity fringes, enabling robust fitting of layer thicknesses, layer compositions and interfacial roughness.

Results

Mixture thermodynamics and interfacial width. PS has been extensively studied in bulk, near surfaces/interfaces and in thin-films (e.g., the dependence of the glass transition temperature on Mw⁴⁰ and film thickness⁴¹), and we have previously utilised this polymer to understand morphological development during OPV fabrication and operation^{42–45}. As part of a recent study on fullerene crystallisation, we uncovered rapid mixing in PS/phenyl-C60-butyric acid methyl ester (PCBM) bilayers in the limit of high PS Mw, well before crystallisation of the fullerene⁴³. Here, we undertake a rigorous test of the hypothesis that such thin-film systems can consistently establish liquid-liquid equilibria between two co-existing amorphous phases (a local equilibrium, representing a metastable situation, before the growth of fullerene crystals), by studying the mixing behaviour as a function of PS Mw, in two different (but closely related) fullerene-based systems (PCBM and bis-adduct phenyl-C60-butyric acid methyl ester (bis-PCBM)).

Domain composition and interfacial structure are of great importance in terms of device performance^{32,46,47} and are also amenable to direct comparison with theory. Experimentally measured compositions in equilibrated co-existing liquid phases in the bulk are usually interpreted using Flory-Huggins mean-field theory, for all-polymer and polymer/small-molecule systems. Theoretical predictions for polymer/polymer interfacial width have been made using mean-field theories^{30,39,48,49}, such as self-consistent-field-theory (SCFT). In the limit of infinite Mw, Helfand and Tagami^{39,48} derived an analytical expression for the equilibrium composition profile at the interface between two

(pure) polymer phases of the form

$$\phi(z) = \frac{1}{2} \left[1 + \tanh \left(\frac{z}{w_1} \right) \right], \quad (1)$$

where $\phi(z)$ is the volume fraction of one of the polymers and z is the distance perpendicular to the interface. The ‘intrinsic’ interfacial width w_1 (due to molecular mixing)^{39,50} is given by

$$w_1 = \frac{b}{\sqrt{6\chi}}, \quad (2)$$

where b is the statistical segment length of the polymers^{39,48} and χ is the Flory-Huggins interaction parameter. Tang and Freed^{39,49} extended this to finite M_w , and produced the following equation to describe w_1 between two polymers, each of degree of polymerisation N

$$w_1(N) = \frac{b}{\sqrt{6\chi}} \left[\frac{3}{4} \left(1 - \frac{2}{\chi N} \right) + \frac{1}{4} \left(1 - \frac{2}{\chi N} \right)^2 \right]^{-\frac{1}{2}}, \quad (3)$$

which shows good agreement with numerical SCFT calculations³⁹. The range of experimental studies on polymer interfaces remains somewhat limited. Reflectivity experiments are sensitive to the (total) interface roughness, which results from the convolution of the intrinsic composition profile, parameterised by w_1 , with any lateral roughness at the interface^{50,51}. Initial measurements of interface roughness at high M_w ^{52,53} were interpreted using a combination of SCFT and capillary-wave theory to model w_1 and lateral roughness respectively, and explain film-thickness-dependent roughness measurements⁵⁰. Interfacial roughness measurements as a function of χ by Chaturvedi et al.⁵⁴ were followed by Carelli et al.⁵⁵ who performed measurements as a function of the degree of immiscibility in a symmetric polymer/polymer bilayer (by tuning either χ or N in the system), and found considerable interface broadening as the system approached criticality. However, to the best of our knowledge, M_w -dependent interface width measurements have not been performed on polymer/small-molecule interfaces.

Equilibration in PCBM/PS as a function of M_w . A summary of the behaviour in annealed PCBM/PS bilayers is shown in Fig. 1a–f. Rapid mixing in polymer/fullerene systems results in metastable states, with the potential for fullerene crystallisation as annealing times and temperatures are increased^{32,43}. We have investigated PCBM crystallisation in PCBM/PS bilayers previously⁴³, finding a strong correlation between the growth of nanoscale crystals (characterised via grazing-incidence X-ray diffraction (GIXD)) and the suppression of large (several microns to tens of microns) needle-like crystal growth, as a function of polymer layer thickness. A typical GIXD pattern produced by such nanoscale crystals is shown in Fig. 1g and a real space image of a needle-like crystal is shown in Fig. 1h. In the present study, much shorter annealing times and lower temperatures were used. No large needle-like crystals were observed on the samples, and GIXD measurements on a broad selection of bilayers (the same samples used for the neutron reflectivity measurements, and also duplicate samples) found scattering patterns that were indicative of amorphous PCBM^{43,56} for all samples, with no evidence of PCBM nanoscale crystal formation (see Fig. 1f and Supplementary Fig. 16). Fig. 1c–e show neutron reflectivity curves, fits and scattering length density (SLD) profiles for a selection of the full PCBM/PS sample set that we measured. These samples cover a range of annealing times, annealing temperatures, PCBM layer thicknesses and M_w . Several unannealed bilayers were also measured (across the range of PS M_w). Full details of and results from the entire sample set are given in the Supplementary Information (Supplementary Notes 1 and 2, and Supplementary

Figs. 1–11). In all fits the SLD profiles were modelled as a bilayer, consisting of two uniform composition layers with Gaussian roughness^{39,50} between the layers. As found in our previous study using PS with weight-average molecular weight (M_w) of 344 kgmol⁻¹,⁴³ the top layer SLD after annealing is significantly above the value for pure PS, due to diffusion of PCBM into the top layer; the mean PCBM volume fraction estimates are between ~8 and 11% in the (originally pure PS) top layers (see Supplementary Notes 1 and 3 for details of the layer SLDs and extracted volume fractions, respectively, for each M_w). In contrast, the SLD of the bottom layer has not changed following annealing (as illustrated schematically in Fig. 1a, and quantified by the SLD profiles before and after the in-situ annealing of a single sample in Fig. 1b). Such strong asymmetry in layer composition, is what one would expect for an equilibrated polymer/small-molecule system, where a polymer-rich phase co-exists with an almost pure small-molecule phase²³ and is in-line with findings for fullerene/polymer blend solutions^{42,57}. Consistent with such SLD changes, is the thinning of the PCBM layer following annealing (without altering the total sample thickness) that is shown in Fig. 1b. Supplementary Note 1 details similar layer thickness changes in ex-situ annealed samples. Figure 1b also shows that the gradient of the line joining the top and bottom layer in the SLD profile is lower after annealing; i.e., the buried (PCBM/PS) interface broadens.

This overall pattern of behaviour (PCBM diffusion into the top layer, preservation of an almost-pure PCBM bottom layer, layer thickness changes and interface broadening) is seen for all M_w s studied (nominal M_w between 2 kg mol⁻¹ and 300 kg mol⁻¹, referred to in the text as 2k, etc). However, as is seen in the SLD profiles in Fig. 1e, there is a systematic difference between the different M_w samples in terms of the width of the buried PCBM/PS-rich interface, showing broader interfaces for lower PS M_w (irrespective of the annealing times or temperatures). It is important to point out that the annealing of ex-situ samples at different temperatures and times is performed in order to ensure that the fullerene diffusion is complete and the composition profile has had enough time to reach equilibrium. Annealing times and temperatures are also important factors in controlling sample quality, as extensive annealing at high temperature for long times can result in lateral inhomogeneities (e.g., from fullerene crystals or dewetting of the polymer layer—especially at low PS M_w). The annealing temperature cannot, however, be used to definitively assess the temperature dependence of the composition profile in this system, because of the potential for changes to this profile during the (albeit rapid) cooling of the samples. The composition profiles that we measure are therefore representative of the frozen-in liquid-liquid system at the point where the system vitrifies on cooling.

The key fit parameters of top layer SLD and buried interface roughness, extracted from the measurements on the ex-situ annealed PCBM/PS sample set, are shown as functions of annealing time and PCBM layer thickness in Fig. 2a, b, and as a function of M_w in Fig. 3a, b. Figure 2a shows that transfer of the PCBM into the PS top layer and interface-broadening occur rapidly (as seen previously in other PCBM bilayers²² and by ourselves in PCBM/PS bilayers at high M_w ⁴³), and that there is no systematic change (beyond the typical sample-sample variation seen in this study) in the samples between 1 and 10 min annealing at 120 °C (the lowest annealing temperature used in the present study). This rapid change followed by stabilisation of the SLD profile, adds support to the proposal, resulting from both ex-situ and in-situ measurements in Mön et al.⁴³ (at high M_w), that the SLD profile represents an equilibrated interface between two co-existing liquid layers. The lack of annealing-time dependence allowed us to perform the majority of the

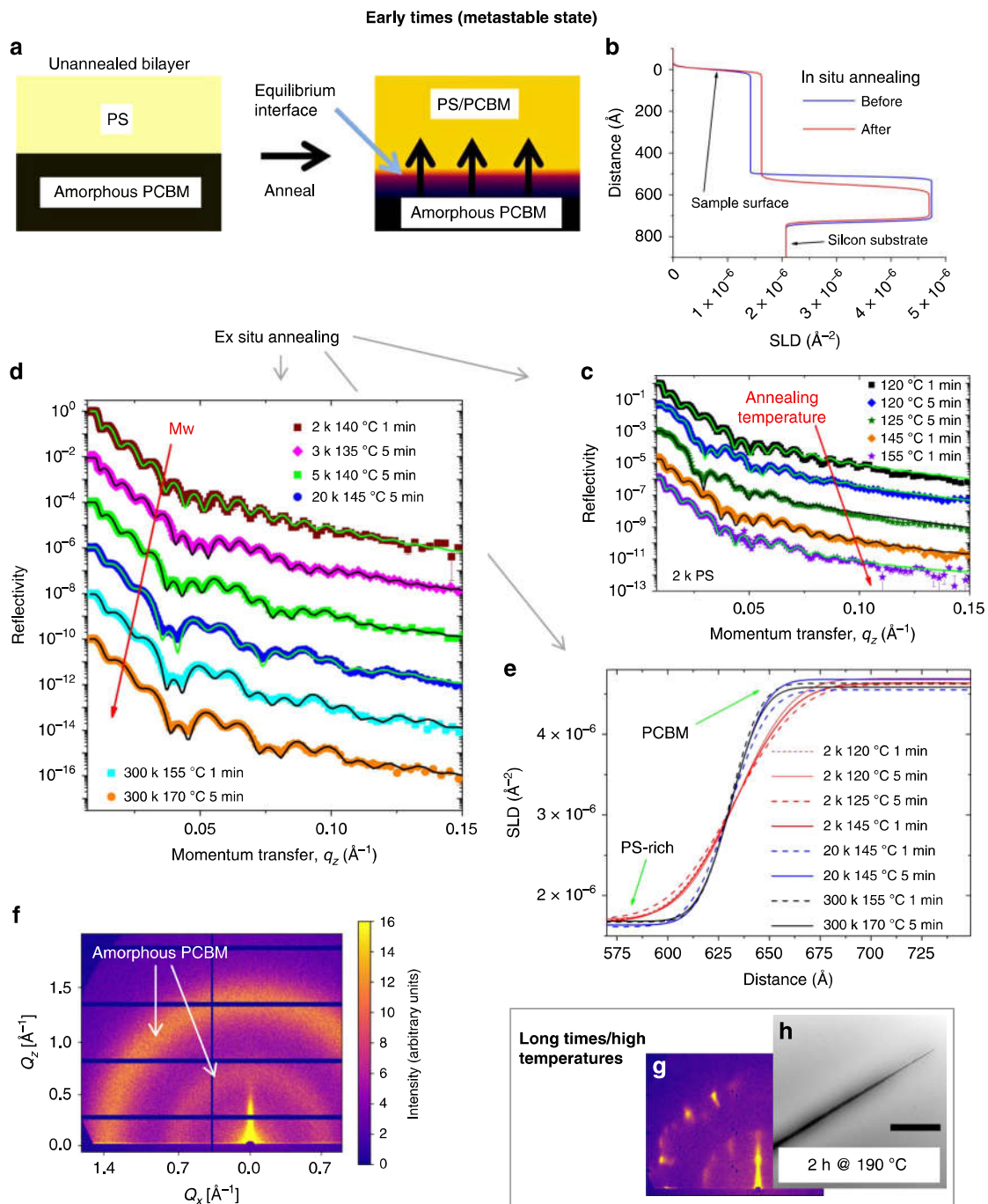


Fig. 1 A summary of the behaviour of PS/PCBM bilayers as a function of PS Mw, annealing time and annealing temperature. **a** A schematic diagram of the rapid diffusion of PCBM into the top (PS) layer. **b** The scattering length density (SLD) profiles from a 5k-PS/PCBM sample before and after annealing (in situ). **c-d** A selection of neutron reflectivity curves and fits (bilayer fits with Gaussian roughness^{39,50} at all interfaces) for a range of different Mw samples annealed for various times at a range of temperatures. Curves are offset vertically for clarity. **e** SLD profiles at the buried PCBM/PS-rich interface, corresponding to fits from a selection of the 2k-PS, 20k-PS and 300k-PS samples. The full SLD profiles, showing the SLDs from the substrate out to the sample surface, along with the corresponding reflectivity data and fits for a further selection of samples are shown in Supplementary Fig. 2. **f** A Grazing-incidence X-ray diffraction GIXD detector map from a typical annealed bilayer (5k-PS/PCBM annealed at 145 °C for 5 min), with the in-plane and out-of-plane components of the momentum transfer represented as Q_x and Q_z , respectively (see Mön et al.⁴³). **g** A GIXD detector map from a crystallised PCBM single layer annealed at higher temperatures and for longer times than used in the present bilayer study (170 °C for 2 h). **h** A transmission electron microscopy image of a PCBM crystal in an annealed 300k PS/PCBM bilayer (scale bar = 3 μm). Apart from the SLD profiles shown in **b**, all data in this figure is from ex-situ annealed samples. The error bars in **c** and **d** are standard deviations, calculated from the neutron count data (error bars that are not visible are smaller than the data symbols)

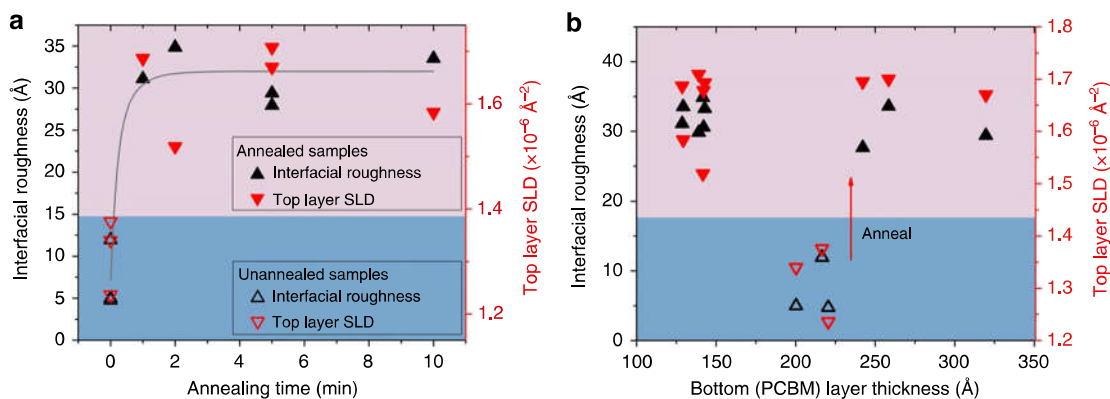


Fig. 2 Bilayer fit parameters as a function of annealing time and PCBM layer thickness for (ex-situ) annealed 2k PS/PCBM bilayers. **a** The (Gaussian) roughness at the buried PCBM/PS interface (left-hand y-axis) and top layer scattering length density (SLD) (right-hand y-axis) versus annealing time at 120 °C. **b** The (Gaussian) interface roughness (left-hand y-axis) and top layer SLD (right-hand y-axis) versus bottom layer thickness (post-annealing thickness). The data points shown as open symbols in **a** and **b** are from three unannealed 2k samples. The grey line in **a** is a guide to the eye for the interfacial roughness measurements. The legends apply to both **a** and **b**

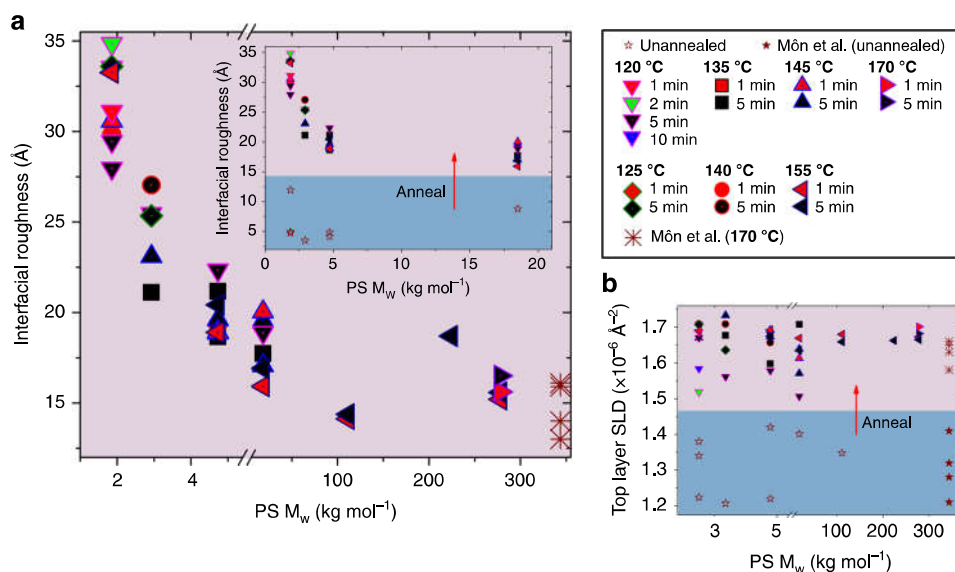


Fig. 3 Bilayer fit parameters for PS/PCBM bilayers annealed (ex-situ) at various temperatures for various times, as a function of the weight-average molecular weight (M_w) of the PS. **a** The (Gaussian) roughness of the buried (PS/PCBM) interfaces in annealed samples. Inset; the same data, but showing the lower M_w samples only, in conjunction with measurements on unannealed samples. **b** The SLD of the top layer in the samples before and after annealing, showing no systematic M_w -dependent behaviour. The data points at 344 kg mol^{-1} in **a** and **b** are from Mön et al.⁴³ (in each plot three of these annealed data points are from samples that were heated for 10 min and the other for 60 min). The legend applies to the data points in both **a** and **b**

measurements on samples that had been annealed for a standard time of 5 min (although equilibration was checked for other M_w samples at various temperatures, by annealing some samples for shorter times). In-situ annealing/neutron reflectivity measurements that were performed on 2–20k PCBM/PS bilayers, also found that the bulk of the PCBM diffusion was concluded within a 5 min period, following a temperature step⁵⁸.

Layer thickness could in-principle influence the measured composition profile in the bilayers. Lateral roughness due to thermal capillary-waves at an equilibrium liquid–liquid interface or liquid surface, will in-principle have a dependence on the thicknesses of the liquid films involved, due to the influence of van der Waals forces on the capillary-wave spectrum⁵⁰. We suspect, however, that this may not be especially significant in our system, due to the absence of significant off-specular scattering, which would be expected to accompany capillary-wave roughness^{51,59}, from the samples (see Supplementary Fig. 11).

We have previously⁴³ examined the influence of the top (PS) layer thickness in PCBM/PS bilayers on composition profiles and on PCBM crystallisation, finding that the thickness of the PS layer did not significantly affect the SLD profiles, in terms of either the layer compositions or the interfacial roughness. Figure 2b shows that the layer composition and interfacial roughness in annealed bilayers also shows no systematic dependence on the thickness of the bottom (PCBM) layer.

Figure 3 shows the top layer SLD and interface roughness for PCBM/PS bilayer samples as a function of M_w , for a range of annealing times and temperatures. As in Fig. 2b, the change in top layer SLD following annealing is clearly evident, as is the lack of any systematic dependence on M_w . The interfacial roughness data, however, show a clear and systematic trend, in which low M_w PS results in a broader interface. This is exactly what you would expect qualitatively, at an equilibrated liquid–liquid interface, due to the higher entropy of mixing of lower M_w

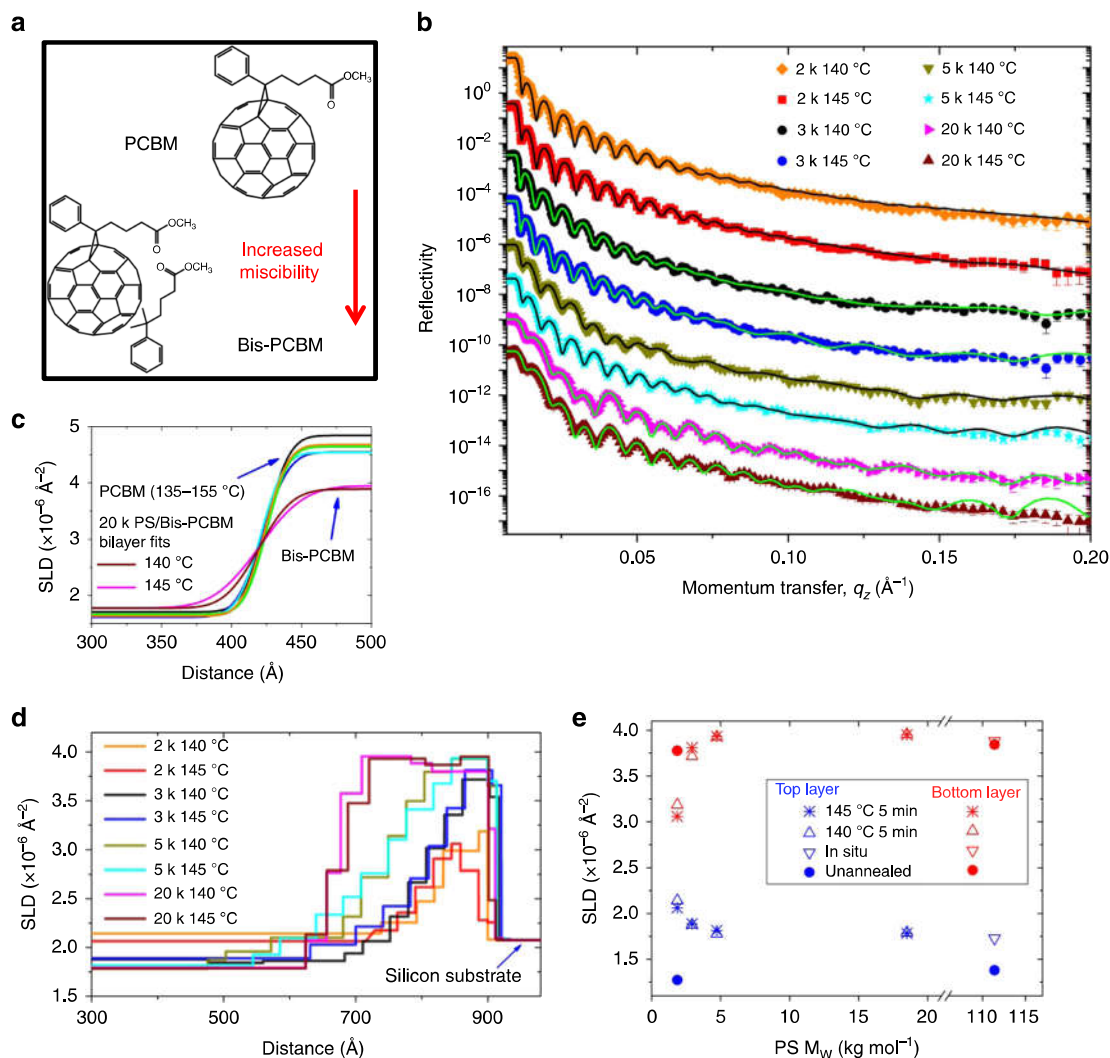


Fig. 4 Neutron reflectivity measurements on bis-PCBM/PS bilayers. **a** Fullerene structures (NB; The second side-chain is not shown attached to the C_{60} cage in bis-PCBM, because the relative positioning of the two side-chains is not precisely controlled, resulting in many isomers⁶⁰). **b** Reflectivity curves and multilayer fits for samples with a range of PS M_w . The data and fits are offset vertically for clarity. **c** Scattering length density (SLD) profiles at the buried (fullerene/PS-rich) interface for bilayer fits (Gaussian interfacial roughness between two uniform layers) to the two 20k-PS/bis-PCBM samples, in comparison to six 20k-PS/PCBM samples (the full SLD profiles and legend for the PS/PCBM samples are shown in Supplementary Fig. 8). The roughness of the 140 °C and 145 °C annealed 20k-PS/bis-PCBM samples in **c** are 25 Å and 35 Å respectively, while those for the 20k-PS/PCBM samples range between 16 Å and 20 Å (see Fig. 3a). NB; The multilayer fits and bilayer fits (not shown) to the reflectivity curves for the 20k-PS/bis-PCBM samples are almost indistinguishable. **d** SLD profiles corresponding to the fits in **b** (the full profiles, showing the SLDs out to the sample surfaces, are shown in Supplementary Fig. 12a). **e** SLD parameters for the top and bottom layers versus the weight-average molecular weight (M_w) of the PS, extracted from the SLD profiles in **d** (the top layer SLD parameters that are plotted here are the maximum values found in the SLD profiles), plus parameters from in-situ annealed and unannealed samples. Except for the in-situ annealed 100k-PS sample, all PS/bis-PCBM samples were annealed (ex-situ) for 5 min. The error bars in **b** are standard deviations, calculated from the neutron count data (error bars that are not visible are smaller than the data symbols)

chains. The magnitude of the observed change is considerable, with around a factor-of-two difference between the mean interface roughness at 2k and at the highest M_w , with most of this difference appearing between 5k and 2k. It is also clear that the sample-to-sample variation in interfacial roughness (measured for samples with various annealing times and temperatures) is smaller than the difference between the measurements at low and higher M_w . Details regarding the robustness and reproducibility of these findings with-respect-to sample preparation, sample measurement and data analysis are given in the Methods and Supplementary Methods.

The impact of fullerene chemistry. To examine the generality of our results, we followed up the PCBM/PS study by investigating

bis-PCBM/PS bilayers. Bis-PCBM is another candidate electron acceptor which has two $C_{12}H_{14}O_2$ side-chains on the C_{60} cage, rather than the single side-chain in PCBM (see Fig. 4a). The additional side-chain simplifies the system by inhibiting crystallisation of this fullerene⁶⁰ and also affects miscibility with solvents and polymers^{20,61,62}. In this system, both bilayer models (with Gaussian interface roughness at the buried interface and surface) and multilayer models (using multiple layers, but with Gaussian roughness at the sample surface only and zero roughness at all internal interfaces) were fitted to the reflectivity data. For each sample, similar SLD profiles were obtained using bilayer or multilayer fits (see Supplementary Fig. 12), but the multilayer models gave better fits (lower values of the ‘goodness-of-fit’ parameter, χ^2 , for all fits). For the lower M_w samples the

‘interface roughness’ parameter extracted from the bilayer fits becomes comparable with the thickness of the lower layer (see Supplementary Fig. 12), and we therefore focus our discussion on the multilayer fits.

In common with our PCBM/PS results and previous measurements of fullerene/amorphous-polymer bilayers^{21,32}, we found no evidence for any preferential segregation of the fullerene at the sample surface (i.e. within the PS-rich top layer—see Supplementary Note 4). This is in contrast to the findings reported for some fullerene/crystallisable-polymer bilayers^{18,21}. Figure 4b–d shows the data, fits and SLD profiles for a set of (ex-situ) annealed bis-PCBM/PS bilayers with Mw between 2k and 20k. A clear and systematic change in the reflectivity curves occurs as the Mw is increased from 2k; the 2k and 3k samples show a single periodicity in the fringes (corresponding to the total sample thickness), with a gradual damping of the fringes with momentum transfer (q_z), whereas at 20k there is clearly more structure to the fringe heights as a function of q_z . The 5k samples show intermediate character. This change is reflected in the SLD profiles, which show a clear bilayer structure (an interface between two uniform layers) for 20k, but a steadily diminishing amount of high SLD material (fullerene) in the bottom ‘layer’, as the Mw reduces. The SLD profile is similar for each of the two duplicate samples made at each Mw, which were annealed at slightly different temperatures. An additional 100k PS sample was also annealed in-situ under vacuum (spending 10 min at a maximum sample surface temperature very similar to that of the 145 °C set-point ex-situ annealed samples; see Supplementary Fig. 15a, b). This sample has an SLD profile that is very similar to the 20k PS samples. For the two 2k samples it is clear that the fullerene molecules initially in the bottom layer have diffused into the top layer in sufficient quantity to raise the SLD of the top layer by a significant amount.

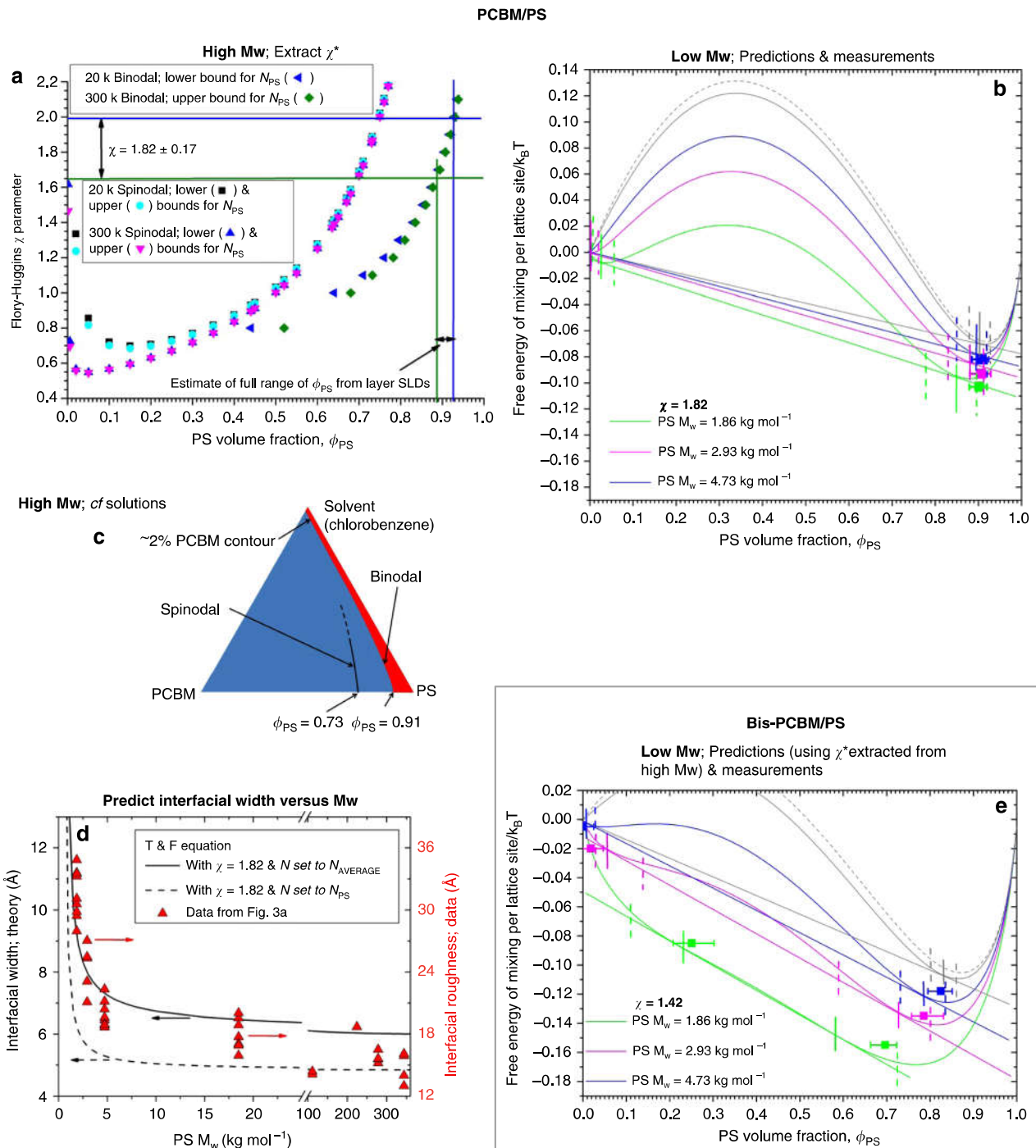
Layer SLDs as a function of Mw are plotted in Fig. 4e. Because of the lack of extensive uniform bottom layers for the lower Mw, Fig. 4e displays the top layer SLD and the maximum value reached in the bottom layer (attained near the substrate); as well as fit parameters from the eight samples in Fig. 4d, Fig. 4e also shows fit parameters from two unannealed bis-PCBM/PS bilayers and the in-situ annealed 100k PS bilayer. Similar to the PCBM/PS system, it is clear that there is diffusion of bis-PCBM into the initially pure PS top layer on annealing, across the Mw range, as evidenced by the increase in SLD (Fig. 4e and Supplementary Fig. 12). At high PS Mw Fig. 4e shows no change in the bottom layer composition on annealing (it remains pure fullerene), as found for PCBM/PS. However, at lower Mw (below 5k) there is a systematic change in this mixing behaviour, in which the SLD of the top layer increases and that of the bottom layer decreases with Mw. Qualitatively, you would expect such increased mixing at lower polymer Mw for a polymer/small-molecule system. We now examine the results for both PCBM/PS and bis-PCBM/PS quantitatively (see Fig. 5a–e), by comparing the experimentally determined volume fractions in each layer (see Supplementary Notes 3 and 5 for calculation details) with the equilibrium predictions of Flory-Huggins mean-field theory (see Supplementary Note 6 for further details), and examining the interfacial roughness measurements in the light of theoretical predictions for equilibrated polymer interfaces.

Quantitative comparison of phase behaviour and interfacial width with Mw. The phase diagram for PCBM/PS shown in Fig. 5a is calculated using the Flory-Huggins free-energy of mixing of a polymer/small-molecule mixture with the number of ‘monomers’ in a chain (N_{PS}) and the χ parameter referenced to the volume of a PCBM molecule. The χ parameter for this system

was extracted using the high Mw (20–300k) layer composition (SLD) data for the annealed PS samples in Fig. 3b. The procedure used to extract χ and an estimate of its uncertainty (see Supplementary Note 6 for further details) involves converting the top layer SLD measurements into volume fractions, incorporating errors in the estimates of the top layer and pure component SLDs. The range of experimentally obtained volume fraction estimates is shown by the vertical green and blue lines in Fig. 5a. These are converted into a χ parameter of 1.82 ± 0.17 using the predicted binodals for the upper and lower estimates of the degree of polymerisation (N_{PS}) of the 20–300k PS chains, (determined by the range of estimates of the pure PS SLD and the PS polydispersity). A similar procedure for bis-PCBM/PS is carried out with-respect-to the data in Fig. 4e (using the 20k and 100k PS data) to extract a phase diagram for bis-PCBM/PS (shown in Supplementary Fig. 14a) and a χ parameter of 1.42 ± 0.14 (here, N_{PS} and χ are referenced to the bis-PCBM molecular volume). Figure 5b plots the calculated free-energy-of-mixing curves for PCBM/PS. The grey curves are the plots for 20k and 100k PS (i.e., two of the Mws that were used to extract χ) and the coloured curves are predictions (with no adjustable parameters) for the lower Mws. The locations of the common tangents to the free energy curves²³, which represent the predicted co-existing compositions at each of the lower Mws, are marked by vertical solid lines, with estimates of the uncertainties in these compositions marked by vertical dashed lines. The solid symbols show the experimentally determined PS volume fractions for each Mw. Figure 5e similarly plots the experimental volume fractions and the free-energy curves for the bis-PCBM/PS system, with N_{PS} and the χ parameter, here referenced to the volume of a bis-PCBM molecule.

For the PCBM/PS system, it is clear from Fig. 5b that the χ parameter required to match the high Mw data, predicts a relatively small change in the PS-rich co-existing composition for the lower Mws used in the study. This is in agreement with the experimental results, in which no systematic Mw dependence is found. The magnitude of the predicted change is not observable given the size of the volume fraction errors and the uncertainty in the location of the co-existing compositions in this system. However, for the bis-PCBM/PS system, it is clear from Fig. 5e that the χ parameter extracted from the high Mw data, predicts a much larger systematic change in the PS-rich coexisting composition as the Mw reduces. For 2k PS the theory also predicts that the co-existing bis-PCBM-rich phase will be significantly below 100% bis-PCBM. This is what is seen experimentally in Fig. 5e (and Fig. 4d, e). Despite the known limitations of Flory-Huggins theory (e.g., due to potential volume changes on mixing and local packing effects)²³ the level of agreement between the predicted behaviour as a function of Mw and the experimental results is actually quite compelling, especially in terms of the magnitude of the changes to both co-existing compositions as the Mw is reduced from 5k to 3k and then to 2k (subject to the increasingly ill-defined nature of the common tangent compositions at around 2k PS, as the curves move closer to criticality).

The effectiveness of Flory-Huggins theory in describing fullerene/PS solutions and subsequently dried films was recently reported for ortho-xylene/PS/[6,6]-phenyl-C71-butyric acid methyl ester mixtures⁵⁷. The binary phase diagram for PCBM/PS (Fig. 5a) is extended into a ternary phase diagram, incorporating blend measurements in chlorobenzene⁴², in Fig. 5c. The asymmetry in these phase diagrams with-respect-to the PCBM/PS ratio can be compared with the morphology of PCBM/PS blends spin-coated from chlorobenzene and then annealed (see Supplementary Fig. 13b–f)⁴⁵. Although care must be taken in drawing inference in relation to the phase diagram from such



non-equilibrium experiments on blends (in which annealing occurs after the traversal of the ternary phase diagram during spin-coating), the asymmetry in the morphological observations (which show a spinodal-like morphology for high PCBM content, but not for high PS content) is consistent with the phase diagrams in Fig. 5a and c. Supplementary Fig. 14a also contains our tentative proposal that the temperature dependence in these PS/fullerene systems is likely to be of an upper-critical-solution-temperature (UCST) form. This proposal is made on the basis of our observations of bis-PCBM/PS bilayers annealed at various temperatures, theoretical expectations (see for example refs. ^{63,64}), and experimental findings from other polymer/solvent and polymer/fullerene systems^{32,63,65} (see Supplementary Note 7 for details).

As stated above, the χ parameter in each system is referenced to the fullerene volume in question. If the χ parameters for the two systems are referenced to the same volume we obtain a ratio of these $\chi_{PCBM/PS}/\chi_{bis-PCBM/PS}$, of 1.7. Dispersion forces are expected to predominate in these systems⁶², giving increased mixing for increased chemical similarity between species. This is evidenced experimentally by the report of increased mixing in polymer/fullerene systems (using polymers with non-conjugated backbones mixed with either C_{60} or PCBM) as side-groups with increasing aromatic character are incorporated within the polymer⁶¹. Also, an increase in chemical similarity in conjugated-polymer/fullerene systems (on moving from bis-PCBM to PCBM) is reported to drive increased mixing²⁰. Therefore on purely energetic grounds our finding of a lower χ parameter for

Fig. 5 Summary of the thermodynamics of PCBM/PS and bis-PCBM/PS. **a** Phase diagram for PCBM/PS showing the binodal and spinodal curves for different values of N_{PS} and the extraction of χ from ϕ_{PS} . The surface temperatures of the samples used to extract χ for PCBM/PS cover the range 117–167 °C. **b** Experimental PCBM/PS volume fraction estimates (solid squares) for three PS Mws (2k, 3k and 5k), extracted from the annealed data in Fig. 3b, plotted in conjunction with the calculated Flory-Huggins free-energy-of-mixing of five of the different Mws used experimentally. The grey curves show the free-energy for 20k and 100k PS bilayers, calculated using a χ parameter of 1.82, referenced to the size of a PCBM molecule, which was extracted using the volume fraction estimates and binodal curves in **a**. The three coloured free-energy curves for lower Mw are predictions for the same value of χ . In both **b** and **e** vertical solid lines indicate the location of the co-existing compositions for each Mw, and vertical dashed lines indicate the uncertainties in these locations. **c** Sketch of the ternary phase diagram for a high-Mw-PS/PCBM/good-solvent (chlorobenzene) system, incorporating our findings for PCBM/PS and the phase boundary in PCBM/PS/chlorobenzene at a few percent solute concentration⁴². **d** Predictions for the intrinsic interfacial width (scale shown on left-hand axis) versus weight-average molecular weight (M_w) for a ‘symmetric’ polymer-polymer interface using the Tang & Freed (T&F) equation (Eq. 3), with $\chi = 1.82$ and an ‘effective’ statistical segment length set to 1.6 nm (see Supplementary Note 6 for further details). The data from Fig. 3a is also plotted here (using the scale shown on the right-hand axis). **e** The same type of plot as in **b**, but for bis-PCBM/PS. Here the experimental data points (solid squares) are extracted from Fig. 4e. The grey curves show the free-energy for 20k and 100k using a χ parameter of 1.42, referenced to the size of a bis-PCBM molecule, which was extracted using Supplementary Fig. 14a. The three coloured free-energy curves for lower Mw are predictions for this value of χ . The surface temperatures of the samples used to extract χ for bis-PCBM/PS cover the range 137–145 °C. The sample surface temperatures quoted in this figure are ~3 degrees C below the set-points for the ex-situ annealed samples (quoted in the text and in Figs. 1–4) and have an uncertainty of ± 2 °C. *NB; Because χ and N_{PS} are referenced to the fullerene molecular size in each particular system, for a given Mw the values of N_{PS} in the two systems are different (N_{PS} values and fullerene volumes are tabulated in the Supplementary Table 1). The calculation of the error bars in **b** and **e** is described in the text. All data in this figure is for ex-situ annealed samples

bis-PCBM/PS compared to PCBM/PS, fits in with a picture of greater chemical similarity in the former system, because of the extra (aromatic containing) solubilising side-chain on the fullerene.

We now discuss the interfacial roughness. Figure 4c shows that the two annealed 20k-PS/bis-PCBM samples have a larger interfacial roughness than all of the annealed 20k-PS/PCBM samples. The ratio of the χ parameters stated above allows us to make a (perhaps rather crude) prediction for the ratio of the interfacial widths in the two systems. SCFT is not quantitatively reliable in small-molecule systems because of the importance of composition fluctuations^{39,66}. However, we are not aware of quantitative predictions for small-molecule/polymer interfaces, and so we proceed by appealing to the SCFT prediction for a polymer-polymer interface in the limit of high Mw, in which the interface width is inversely proportional to the square-root of χ (Eq. (2))^{39,48}. This predicts a 30% broader interface for a purely polymeric system with a χ parameter equal to that of the bis-PCBM/PS system in comparison to a purely polymeric system with a χ parameter equal to that of the PCBM/PS system. Averaging the interfacial roughness measurements between 20k and 100k PS for the three bis-PCBM/PS samples that were annealed at 140–145 °C (see Supplementary Fig. 15g), and for the PCBM/PS system (averaging from 20k to 300k in Fig. 3a), results in values of 29 ± 3 Å and 16.9 ± 0.5 Å respectively, which has a ratio of 1.7 ± 0.2 . This is somewhat higher than a 30% difference, but is clearly of the same order. Comparisons can also be made between our measurements and predictions for interfacial width as a function of the degree of polymerisation, N . Figure 5d shows the behaviour for ‘symmetric’ polymeric systems (i.e., polymer bilayers with the same value of N in each layer) according to Tang and Freed^{39,49} (Eq. (3)), that is predicted using the χ parameter extracted from the PCBM/PS layer composition measurements. It is not clear that this approach should be at all valid for our polymer/small-molecule interfaces, given the potential importance of fluctuations^{39,66}, and it is also not clear which value should be taken for N . However, our aim here is to obtain an order-of-magnitude estimate of the potential impact of polymer Mw on the interfacial width, and we therefore plot the Tang and Freed model using two different values for N . Firstly we take N as simply the degree of polymerisation of the PS chains, N_{PS} , and secondly we use the value of $N_{AVERAGE}$ defined as $4(1 + N_{PS}^{-1/2})^{-2}$, which is the key parameter in determining miscibility in a polymer/small-molecule system (further details in

Supplementary Note 6)²³. There are no adjustable parameters in these plots.

If we take the experimental data in Fig. 3a as being due solely to molecular level mixing (i.e., with no lateral roughness due to capillary-waves), it is clear that in comparison to the predictions in Fig. 5d the magnitude of the measurements (right-hand y-axis) is larger than the predictions (left-hand y-axis) by around a factor of 3-to-4. This magnitude of discrepancy is in contrast to Sferazza et al.⁵⁰ for high Mw polymer/polymer interfaces (where mean-field theory is valid), who report much closer agreement between the predictions of SCFT and their deduced intrinsic interface width. Sferazza et al. used theoretical predictions to account for a capillary-wave contribution to the interface roughness that they measured by specular reflectivity, which turned out to be of the same order as the intrinsic interfacial width. While capillary-wave roughness could in-principle contribute to our measured roughness, a more significant aspect of the discrepancy in PCBM/PS may result from a contribution to the measured width due to composition fluctuations within our small-molecule/polymer system (this will be averaged over the in-plane coherence length of the neutrons, which is on the order of microns or larger^{50,67}). However, despite the clear discrepancy between the magnitude of our measurements and the Tang and Freed equation, the Mw dependence is rather reasonable (for both definitions of N plotted in Fig. 5d), in terms of the Mw below which significant changes occur and the actual size of the change in width with Mw (in terms of percentage changes with Mw). Perhaps the relatively large size of the fullerene ‘small-molecules’ (and other small-molecule acceptors) is a significant factor here, causing averaging over a large enough volume to produce Mw-dependent behaviour that scales reasonably well with the mean-field prediction.

The absence of significant off-specular scattering from the bilayers deserves a comment here. This absence implies that lateral roughness due to long wavelength capillary-waves (typically of order microns) may not be that significant in the systems we have studied. However, one could ask the question; ‘if composition fluctuations (within the PS-rich layer) were important, would we not expect to see some kind of signature of this in the off-specular scattering?’ An important consideration, however, is that it may actually be entirely reasonable for fluctuations to be contributing to the measured interfacial widths, but not leave any significant trace in the off-specular scattering. Typical correlation lengths in polymer blends and solutions are

on the order of a few nm to tens of nm²³, with a recently reported value for a (miscible) blend of around 10%-PCBM in PS (by volume) equal to 60 ± 40 nm⁶¹. However, the in-plane distances to which off-specular neutron scattering is sensitive are on the order of a few hundred nm to a few microns⁵¹. This means that in-plane fluctuations on the size-scale of the correlation length or lower will not show up in the off-specular scattering, but such fluctuations normal to the substrate may affect the specular reflectivity and contribute to the measured interfacial roughness.

In summary, the hypothesis that polymer/fullerene thin-film systems can form composition profiles consisting of two co-existing phases in liquid-liquid equilibrium, has been robustly confirmed in this work, with a series of neutron reflectivity experiments on model bilayer systems (PS/PCBM and PS/bis-PCBM) across an unprecedented parameter space of polymer mass, annealing temperature, annealing time and layer thickness. Theoretical predictions of the effect of polymer Mw on layer composition and interface width, solely based on composition measurement in the high Mw limit, are found to be in remarkable agreement with data. Specifically, the PS/PCBM series shows marginal changes in layer composition with polymer Mw, by contrast with the PS/bis-PCBM series for which composition variations with Mw (directly computed from layer SLD) are significant. In both systems, a significant increase in interfacial width upon decreasing Mw is observed, as expected from equilibrium thermodynamics. This equilibration process occurs rapidly upon annealing (at shorter timescales than the measurement resolution of the order of minutes), and well before fullerene crystallisation timescales.

Discussion

The fact that changes in layer composition and fractional changes in interfacial width with Mw, in the PS/fullerene systems that we have studied, can be accounted for in a quantitative way (with-respect-to the layer compositions) or in a semi-quantitative way (with-respect-to the interface width behaviour with Mw) by mean-field theories is remarkable. It is hoped that this ability to successfully apply equilibrium thermodynamics to these model systems will contribute to greater understanding and predictive ability in a broad range of fullerene and other small-molecule containing OPV systems. The significance of the region of phase-space that is explored in the current study in relation to working devices, was recently emphasised by the report of 'ideal' miscibility (near the fullerene percolation threshold) leading to optimum device performance in polymer/fullerene OPVs at compositions of ~10–20% fullerene³⁴.

While the ability to predictively engineer OPV active layer morphology has been so far limited, there is growing evidence that equilibrium thermodynamics such as the Flory-Huggins lattice theory can, despite its many shortcomings, capture significant aspects of component miscibility and even performance³². Our study now unequivocally shows that polymer Mw can be employed as an effective approach to tune phase composition and interfacial width between coexistent phases of polymer/fullerene mixtures, which we find are well described by Flory-Huggins theory and SCFT. Our approach is applicable to a broad range of material combinations in which amorphous mixed phases are found, spanning amorphous and semi-crystalline polymers, non-fullerene small-molecule acceptors and all-polymer blends; as well as enabling the extraction of key parameters such as χ , liquid-liquid equilibria are also significant in terms of device stability, as they represent the state towards which amorphous domain compositions and interfaces, given sufficient molecular mobility, can evolve over time^{13,36}.

Care must be taken when determining χ in the presence of extensive crystallisation; while it is the amorphous (liquid-liquid) χ parameter (χ_{aa} in the nomenclature of Ye et al.³²) that is reported to control device performance, Flory-Huggins theory needs to be extended to account for extensive crystallisation and enable the correct extraction of χ under these circumstances³². In the case of a device made from a blend of a small-molecule acceptor and a semi-crystalline polymer, you would also expect that extensive crystallisation would cause the polymer crystal surface to exhibit significant roughness. However, even near the polymer crystallites, it is likely that the molecular mixing, that will be a key influence on the photophysics at heterojunctions^{46,47,68}, will be largely governed by the mixing between the small-molecules and amorphous chain segments that protrude from the surface of the crystallites⁶⁹.

Evidently, aspects of OPV morphology, such as domain-composition, domain-size, shape and connectivity, interfacial-mixing, crystalline-fraction and preferential segregation of components to interfaces, can in principle be understood by a combination of equilibrium thermodynamics and kinetics. Based on the framework reported herein, and based on relatively straightforward measurements of bilayer composition at thermal equilibrium (such as those obtained by ellipsometry²⁰), comprehensive parameter-free predictions for composition and interfacial width can be obtained across a broad range of polymer dimensions (Mw). While, conjugated polymers employed in OPV devices generally exhibit broad size distributions, our study with narrow polymer standards enables direct quantification of the role of polymer size, otherwise rather elusive due to interfacial segregation of and varying mobility of polymer fractions of different dimensions.

We expect that the interfacial width behaviour that we report for narrow Mw-distribution polymers represents a lower-limit in relation to polydisperse systems (due to enhanced segregation of low Mw fractions to the interface). A current limitation to our approach is that the ability to fully quantify interfacial width in polydisperse polymer/small-molecule systems (rigorously accounting for the scale-factor difference between theory and measurement, and also assessing the impact of realistic Mw distributions on the width), requires further theoretical/computational attention. Given the key importance of these kinds of interfaces we strongly believe that such attention is warranted. The approach reported herein can, however, be extended to enable the analysis of equilibrium phase compositions in polydisperse polymers. Our methodology allows assessment of whether conjugated polymer/small-molecule mixtures contain Mw fractions for which one would expect Mw-dependent behaviour. In the presence of such low Mw fractions, Flory-Huggins theory can, if required, be adapted to include the effects of broad Mw distributions on phase coexistence (modifying the polymer/small-molecule volume fractions of the coexisting phases and also describing potential fractionation of the polymers by Mw, with-respect-to these phases)^{27,28}. In conclusion, we expect that the behaviour elucidated in this study can complement material synthesis and device optimisation efforts, and contribute to rational design of continually improved, stable, high performance OPVs, and also serve as a catalyst for further investigations of the polymer physics of these technologically important interfaces.

Methods

Materials. PCBM and bis-PCBM with a purity of 99.5% were purchased from Solenne, Netherlands. Seven different PS batches were purchased from Agilent Technologies, UK. The nominal molecular weights of these were 2, 3, 5, 20, 100, 200 and 300 kg mol⁻¹. The weight-average molecular weights (M_w) of these batches were 1.86, 2.93, 4.73, 18.5, 111.4, 224.2 and 278.2 kg mol⁻¹ respectively, with polydispersity indices (M_w/M_n , where M_n is the number-average molecular weight) of 1.04, 1.04, 1.04, 1.03, 1.03, 1.03 and 1.05 respectively. These batches are referred

to as 2k, 3k, etc throughout this paper. Silicon substrates of orientation 100 (with a native oxide layer), with a diameter of 2 inches and a thickness of 1150 microns were purchased from Siltronix, France. Mica sheets of size 65 × 65 mm and thickness 0.15 mm were purchased from Goodfellow, UK. Toluene, chlorobenzene, acetone and isopropanol (all of purity 99.9%) were all purchased from Sigma Aldrich, UK.

Sample fabrication. Fullerenes were dissolved in chlorobenzene and then spin-coated onto silicon substrates that had been sonicated in acetone and isopropanol (for 15 min each) and then rinsed in de-ionised water. The PS layers were spin-coated from toluene solutions onto freshly cleaved mica substrates, and then floated on top of the silicon/fullerene in a bath of de-ionised water (further details in Mon et al.⁴³ and Hynes⁵⁸). The samples were then placed under vacuum at room temperature (and in the dark) for at least 2 h. Samples were then stored in the dark, and were annealed within a few days of fabrication.

Sample annealing. Samples were annealed (ex-situ) in the dark for various times, in a vacuum oven (Binder, Germany) and then rapidly cooled onto a metal block. In-situ annealing was performed under vacuum in the neutron beam at D17, ILL, France. Unless stated otherwise the temperatures quoted in the main text and figures are the nominal (set-point) temperatures. There is an offset between these temperatures and the sample surface temperatures of a few °C (see Supplementary Methods for details).

Neutron reflectivity. The time-of-flight (TOF) methodology in which a broad range of wavelengths is incident on the sample was used for all neutron reflectivity measurements. Two reflectometers (D17⁷⁰ and Figaro⁷¹) at the Institut Laue Langevin (ILL), Grenoble, France were used. Both D17 and Figaro use an area detector (with an incident ‘ribbon’ beam), enabling the collection of off-specular scattering. We also used Inter at ISIS at the Rutherford Appleton Laboratory, UK, but this time with a point detector that only collects the specularly reflected neutrons (but still utilising an incident ‘ribbon’ beam). Two incident angles were used at all three instruments. Neutrons were counted for 10 min at the lower incident angle of 0.72° and 75 min at the higher angle of 2.71° at Figaro. The instrumental resolution (dq_z/q_z) at Figaro varied from 2.9% to 3.9% with increasing q_z (from ~ 0.007 to 0.2 \AA^{-1}). At D17 the first and second angles of 0.8° and 3.2° were measured for 15 and 80 min (the instrumental resolution here varied from 1.7% to 5.8% across the q_z range). At Inter the first and second angle of 0.5° and 2° were measured for 15 min and either 45 or 90 min, respectively. The samples were under-illuminated for both the D17 and Figaro measurements and over-illuminated at Inter. To calculate the specular reflectivity curves from the raw data obtained from the incident and reflected neutron beams at the ILL, we used the COSMOS data reduction program⁷². A data-reduction code written in Python at ISIS was used to produce reflectivity curves from the raw data from Inter. In the data analysis a fixed percentage resolution (fixed dq_z/q_z) was chosen for each instrument. The value used reflects a combination of the instrumental resolution (set by the slit geometry and chopper settings of the instruments) and any effective resolution effects that may occur due to the samples themselves, such as over-illumination of the sample, in which the sample itself will tend to improve the effective resolution of the experiment, or slight layer thickness variation across the samples which will tend to reduce the resolution of the sharpest minima in the reflectivity curve. The resolution was fixed for the entire batch of samples measured on each particular instrument. Resolutions ($dq_z/q_z \times 100$) of 3.5%, 4% and 5% were used when fitting the samples measured at Inter, D17 and Figaro, respectively. As well as using a constant dq_z/q_z resolution, a selection of the Figaro and D17 samples were also fitted with the resolution set equal to the (varying) instrumental resolution. These fits gave a higher value of χ^2 for all selected samples, but the fit parameters themselves were rather insensitive to changes in the resolution; in going from constant to varying dq_z/q_z resolution the Figaro and D17 layer SLD parameters changes by a maximum of $0.05 \times 10^{-6} \text{ \AA}^{-2}$ and the interface roughness by a maximum of 1.2 Å.

Reflectivity curves were fitted using motofit⁷³ with either; (i) bilayer models with Gaussian roughness at the buried fullerene/PS-rich interfaces and the sample surface, or (ii) multilayer models with zero roughness between all buried layers within the sample and a Gaussian sample surface roughness. Bilayer fits of the neutron reflectivity data involved 6 adjustable parameters; the SLD and thickness of each layer, the interfacial roughness, and the sample surface roughness. Multilayer models had between 6 and 12 layers, and so had a much larger number of adjustable parameters (two per layer; thickness and SLD) than the bilayer models. Since simpler models are preferable, multilayer models were only necessary when bilayer models failed to fit the data well, as in the case of the 2k, 3k, and 5k PS/bis-PCBM bilayers (as evidenced by the increasing differences between the SLD profiles for the multilayer and bilayer fits in Supplementary Fig. 12b-g, as the Mw reduces, but the close correspondence between bilayer and multilayer fits in Supplementary Fig. 12h-i). There is also a silicon oxide layer, which is not adjustable; this is fixed in the model for each batch of silicon samples (silicon substrates fabricated in the same batch and measured on the same instrument; see Supplementary Methods for details). The layer thicknesses and layer SLD parameters (and surface/interface roughnesses for the bilayer fits) were not

constrained during fitting. Nevertheless excellent conservation of the total sample thickness was found for those samples measured before and after (in-situ) annealing for both PS/PCBM and PS/bis-PCBM (see Fig. 1b and Supplementary Fig. 15b respectively). For the bilayer PS/PCBM fits, in which the Gaussian roughness represents the width of the error function SLD profile at the sample surface and buried interface, it was also necessary to check that surface and interface roughness parameters returned by the fits remained small in comparison to the layer thicknesses within the sample. This was most significant for the thinner bottom (fullerene) layers; for all PS/PCBM samples the bottom layer thickness was a factor of at least 3.8 times larger than the Gaussian roughness of the buried interface (see for example Fig. 2b). The robustness of the reflectivity measurements and the extracted fit parameters was investigated in a number of ways, including performing repeat measurements, assessing the quality of the samples using real space (imaging) methods and carefully examining the robustness of the fitting procedures. Further data from the complete sample set used in this study, further details of the data reduction and analysis and a summary of the robustness tests regarding the extracted fit parameters are given in the Supplementary Information (Supplementary Figs. 1–12, 15, 19–21, Supplementary Notes 1-5 and Supplementary Methods). Further discussion of the data reduction, data analysis and robustness tests can also be found in Hynes⁵⁸.

Grazing-incidence X-ray diffraction (GIXD). Measurements were performed at Sheffield University and at Diamond Light Source. The measurements at Sheffield were taken using a Xeuss 2.0 (Xenocs France) small-angle X-ray scattering/wide-angle X-ray scattering laboratory beamline, with a liquid gallium MetalJet X-ray source (Excillum Sweden) which has an X-ray energy of 9.2 keV and a corresponding wavelength of 1.34 Å. The instrument was calibrated using silver behenate (Alfa Aesar). The sample chamber and flight tubes were all evacuated to reduce air scatter. The X-rays were detected using a Pilatus3R 1 M detector. The measurements at Diamond utilised beamline I07 with a 10.5 keV X-ray beam focused onto the samples at a range of grazing incidence angles between 0 and 0.5°. The samples were mounted inside the helium filled I07 grazing incidence sample chamber. X-ray scattering images were captured with a Pilatus 2 M detector at a camera length of 293 mm, calibrated using a silver stearate sample. The maps shown (see Supplementary Note 8 and Supplementary Fig. 16) are direct detector maps, as presented by previous workers⁵⁶, with the axis labels Q_z and Q_x representing the out-of-plane and in-plane components of the momentum transfer respectively (see the supplementary information of Mõn et al.⁴³ for definitions).

Fourier transform infrared spectroscopy. Spectra were collected to check the quality of the samples with-respect-to potential degradation of the materials during thermal annealing. No evidence of oxidation of either the PS or fullerenes was found (see Supplementary Methods and Supplementary Fig. 18 for details).

Transmission electron microscopy. Samples were prepared by spin-coating PCBM layers onto cleaved mica, rather than silicon substrates. Bilayers were then fabricated and annealed in the same way as on silicon substrates. After annealing, the samples were floated onto the surface of de-ionised water and picked up on grids (Agar Scientific, UK) with and without a holey-carbon support film. Images were obtained using a Field-Emission-Gun-Transmission-Electron Microscope (FEI Tecnai TF20) operated at 200 kV with a CCD Camera (Gatan Orius SC600A).

Statistics. Except for the uncertainty estimates for the Flory-Huggins χ parameters in the PC/PCBM and PS/bis-PCBM systems and the error bars in the neutron reflectivity plots, all errors plotted in figures or given in the text are standard errors. The calculation of the uncertainty estimates for χ are described in the text and in Supplementary Note 6, and the error bars in the neutron reflectivity plots represent the standard deviation (calculated from the neutron counts).

Data availability

Data is available from the corresponding author upon request. The raw neutron reflectivity data is stored on databases at ISIS and ILL in the following locations; doi:10.5291/ILL-DATA.9-12-387 (Figaro); doi:10.5291/ILL-DATA.9-12-456 (D17); doi:10.5286/ISIS.E.83549212 and doi:10.5286/ISIS.E.85421152 (Inter).

Received: 20 December 2018 Accepted: 14 August 2019

Published online: 16 September 2019

References

- Zhao, F. et al. Single-junction binary-blend nonfullerene polymer solar cells with 12.1% efficiency. *Adv. Mater.* **29**, 1700144 (2017).
- Zhao, W. et al. Molecular optimization enables over 13% efficiency in organic solar cells. *J. Am. Chem. Soc.* **139**, 7148–7151 (2017).

3. Hou, J., Inganas, O., Friend, R. H. & Gao, F. Organic solar cells based on nonfullerene acceptors. *Nat. Mater.* **17**, 119–128 (2018).
4. Fan, Q. et al. Chlorine substituted 2D-conjugated polymer for high-performance polymer solar cells with 13.1% efficiency via toluene processing. *Nano Energy* **48**, 413–420 (2018).
5. He, D. et al. A fused ring electron acceptor with decacyclic core enables over 13.5% efficiency for organic solar cells. *Adv. Energy Mater.* **8**, 1802050 (2018).
6. Xiong, Y. et al. Revealing the impact of F4-TCNQ as additive on morphology and performance of high-efficiency nonfullerene organic solar cells. *Adv. Funct. Mater.* **29**, 1806262 (2019).
7. Ye, L. et al. Quenching to the percolation threshold in organic solar cells. *Joule* **3**, 443–458 (2019).
8. Ye, L. et al. Surpassing 10% efficiency benchmark for nonfullerene organic solar cells by scalable coating in air from single nonhalogenated solvent. *Adv. Mater.* **30**, 1705485 (2018).
9. Xiao, Z., Jia, X. & Ding, L. Ternary organic solar cells offer 14% power conversion efficiency. *Sci. Bull.* **62**, 1562–1564 (2017).
10. Meng, L. et al. Organic and solution-processed tandem solar cells with 17.3% efficiency. *Science* **361**, 1094–1098 (2018).
11. Huang, Y., Kramer, E. J., Heeger, A. J. & Bazan, G. C. Bulk heterojunction solar cells: morphology and performance relationships. *Chem. Rev.* **114**, 7006–7043 (2014).
12. Heeger, A. J. 25th anniversary article: bulk heterojunction solar cells: understanding the mechanism of operation. *Adv. Mater.* **26**, 10–27 (2014).
13. Li, N. et al. Abnormal strong burn-in degradation of highly efficient polymer solar cells caused by spinodal donor-acceptor demixing. *Nat. Commun.* **8**, 14541 (2017).
14. Vandewal, K., Himmelberger, S. & Salbeck, J. Structural factors that affect the performance of organic bulk heterojunction solar cells. *Macromolecules* **46**, 6379–6387 (2013).
15. Kiel, J. W., Eberle, A. P. & Mackay, M. E. Nanoparticle agglomeration in polymer-based solar cells. *Phys. Rev. Lett.* **105**, 168701 (2010).
16. Bartelt, J. A. et al. The importance of fullerene percolation in the mixed regions of polymer-fullerene bulk heterojunction solar cells. *Adv. Energy Mater.* **3**, 364–374 (2013).
17. Chen, D., Nakahara, A., Wei, D., Nordlund, D. & Russell, T. P. P3HT/PCBM bulk heterojunction organic photovoltaics: correlating efficiency and morphology. *Nano Lett.* **11**, 561–567 (2011).
18. Chen, H., Hegde, R., Browning, J. & Dadmun, M. D. The miscibility and depth profile of PCBM in P3HT: thermodynamic information to improve organic photovoltaics. *Phys. Chem. Chem. Phys.* **14**, 5635–5641 (2012).
19. Collins, B. A. et al. Molecular miscibility of polymer-fullerene blends. *J. Phys. Chem. Lett.* **1**, 3160–3166 (2010).
20. Lemam, D. et al. In situ characterization of polymer-fullerene bilayer stability. *Macromolecules* **48**, 383–392 (2015).
21. Ro, H. W. et al. Poly(3-hexylthiophene) and [6,6]-Phenyl-C61-butyric acid methyl ester mixing in organic solar cells. *Macromolecules* **45**, 6587–6599 (2012).
22. Treat, N. D. et al. Interdiffusion of PCBM and P3HT reveals miscibility in a photovoltaically active blend. *Adv. Energy Mater.* **1**, 82–89 (2011).
23. Rubinstein, M. & Colby, R. H. in *Polymer Physics*. (Oxford University Press, Oxford, 2003).
24. Deshmukh, K. D. et al. Tuning the molecular weight of the electron accepting polymer in all-polymer solar cells: impact on morphology and charge generation. *Adv. Funct. Mater.* **28**, 1707185 (2018).
25. Wadsworth, A. et al. Progress in poly(3-hexylthiophene) organic solar cells and the influence of its molecular weight on device performance. *Adv. Energy Mater.* **8**, 1801001 (2018).
26. Kingsley, J. W. et al. Molecular weight dependent vertical composition profiles of PCDTBT:PC71BM blends for organic photovoltaics. *Sci. Rep.* **4**, 05286 (2014).
27. Sollich, P. & Cates, M. E. Projected free energies for polydisperse phase equilibria. *Phys. Rev. Lett.* **80**, 1365–1368 (1998).
28. Warren, P. B. Combinatorial entropy and the statistical mechanics of polydispersity. *Phys. Rev. Lett.* **80**, 1369–1372 (1998).
29. Schichtel, T. E. & Binder, K. Kinetics of phase separation in polydisperse polymer mixtures. *Macromolecules* **20**, 1671–1681 (1987).
30. Broseta, D., Fredrickson, G. H., Helfand, E. & Leibler, L. Molecular-weight and polydispersity effects at polymer-polymer interfaces. *Macromolecules* **23**, 132–139 (1990).
31. Mahmoudi, P., Forrest, W. S. R., Beardsley, T. M. & Matsen, M. W. Testing the universality of entropic segregation at polymer surfaces. *Macromolecules* **51**, 1242–1247 (2018).
32. Ye, L. et al. Quantitative relations between interaction parameter, miscibility and function in organic solar cells. *Nat. Mater.* **17**, 253–260 (2018).
33. Yin, W. & Dadmun, M. A new model for the morphology of P3HT/PCBM organic photovoltaics from small-angle neutron scattering: rivers and streams. *ACS Nano* **5**, 4756–4768 (2011).
34. Ye, L. et al. Miscibility-function relations in organic solar cells: significance of optimal miscibility in relation to percolation. *Adv. Energy Mater.* **8**, 1703058 (2018).
35. Yang, D. et al. Stable efficiency exceeding 20.6% for inverted perovskite solar cells through polymer-optimized PCBM electron-transport layers. *Nano Lett.* **19**, 3313–3320 (2019).
36. Liu, Y. et al. Aggregation and morphology control enables multiple cases of high-efficiency polymer solar cells. *Nat. Commun.* **5**, 5293 (2014).
37. Xiao, M. et al. High-performance ternary nonfullerene polymer solar cells with both improved photon harvesting and device stability. *ACS Appl. Mater. Interfaces* **10**, 25594–25603 (2018).
38. Composto, R. J., Mayer, J. W., Kramer, E. J. & White, D. M. Fast mutual diffusion in polymer blends. *Phys. Rev. Lett.* **57**, 1312–1315 (1986).
39. Jones, R. A. L. & Richards, R. W. in *Polymers at Surfaces and Interfaces*. (Cambridge University Press, Cambridge, 1999).
40. Santangelo, P. G. & Roland, C. M. Molecular weight dependence of fragility in polystyrene. *Macromolecules* **31**, 4581–4585 (1998).
41. Ediger, M. D. & Forrest, J. A. Dynamics near free surfaces and the glass transition in thin polymer films: a view to the future. *Macromolecules* **47**, 471–478 (2013).
42. Dattani, R. & Cabral, J. T. Polymer fullerene solution phase behaviour and film formation pathways. *Soft Matter* **11**, 3125–3131 (2015).
43. Mön, D. et al. Bimodal crystallization at polymer-fullerene interfaces. *Phys. Chem. Chem. Phys.* **17**, 2216–2227 (2015).
44. Wong, H. C., Higgins, A. M., Wildes, A. R., Douglas, J. F. & Cabral, J. T. Patterning polymer-fullerene nanocomposite thin films with light. *Adv. Mater.* **25**, 985–991 (2013).
45. Pont, S., Foglia, F., Higgins, A. M., Durrant, J. R. & Cabral, J. T. Stability of polymer:PCBM thin films under competitive illumination and thermal stress. *Adv. Funct. Mater.* **28**, 1802520 (2018).
46. Sreearunothai, P. et al. Influence of copolymer interface orientation on the optical emission of polymeric semiconductor heterojunctions. *Phys. Rev. Lett.* **96**, 117403 (2006).
47. Yan, H. et al. Influence of annealing and interfacial roughness on the performance of bilayer donor/acceptor polymer photovoltaic devices. *Adv. Funct. Mater.* **20**, 4329–4337 (2010).
48. Helfand, E. & Tagami, Y. Theory of the interface between immiscible polymers II. *J. Chem. Phys.* **56**, 3592–3601 (1972).
49. Tang, H. & Freed, K. F. Interfacial studies of incompressible binary blends. *J. Chem. Phys.* **94**, 6307–6322 (1991).
50. Sferrazza, M. et al. Evidence for capillary waves at immiscible polymer/polymer interfaces. *Phys. Rev. Lett.* **78**, 3693–3696 (1997).
51. James, D. et al. Measurement of molecular mixing at a conjugated polymer interface by specular and off-specular neutron scattering. *Soft Matter* **11**, 9393–9403 (2015).
52. Anastasiadis, S. H., Russell, T. P., Satija, S. K. & Majkrzak, C. F. The morphology of symmetric diblock copolymers as revealed by neutron reflectivity. *J. Chem. Phys.* **92**, 5677–5691 (1990).
53. Fernandez, M. L. et al. Neutron reflection investigation of the interface between an immiscible polymer pair. *Polymer* **29**, 1923–1928 (1988).
54. Chaturvedi, U. K., Steiner, U., Zak, O., Krausch, G. & Klein, J. Interfacial structure in polymer mixtures below the critical point. *Phys. Rev. Lett.* **63**, 616–619 (1989).
55. Carelli, C. et al. Approaching criticality in polymer-polymer systems. *Phys. Rev. E* **72**, 031807 (2005).
56. Verploegen, E. et al. Effects of thermal annealing upon the morphology of polymer-fullerene blends. *Adv. Funct. Mater.* **20**, 3519–3529 (2010).
57. van Franeker, J. J. et al. Sub-micrometer structure formation during spin coating revealed by time-resolved in situ laser and X-ray scattering. *Adv. Funct. Mater.* **27**, 1702516 (2017).
58. Hynes, E. L. Mixing and Interfacial Composition in Polymer/fullerene Thin Films. PhD thesis, Swansea University (2018).
59. Sinha, S. K., Sirota, E. B., Garoff, S. & Stanley, H. B. X-ray and neutron-scattering from rough surfaces. *Phys. Rev. B* **38**, 2297–2311 (1988).
60. Bouwer, R. K. M., Wetzelaer, G.-J. A. H., Blom, P. W. M. & Hummelen, J. C. Influence of the isomeric composition of the acceptor on the performance of organic bulk heterojunction P3HT:bis-PCBM solar cells. *J. Mater. Chem.* **22**, 15412–15417 (2012).
61. Bernardo, G., Deb, N., King, S. M. & Bucknall, D. G. Phase behavior of blends of PCBM with amorphous polymers with different aromaticity. *J. Poly. Sci. Part B* **54**, 994–1001 (2016).
62. Perea, J. D. et al. Combined computational approach based on density functional theory and artificial neural networks for predicting the solubility parameters of fullerenes. *J. Phys. Chem. B* **120**, 4431–4438 (2016).
63. Jiménez-Serratos, G., Herdes, C., Haslam, A. J., Jackson, G. & Müller, E. A. Group contribution coarse-grained molecular simulations of polystyrene melts and polystyrene solutions in alkanes using the SAFT- γ force field. *Macromolecules* **50**, 4840–4853 (2017).

64. Paricaud, P., Varga, S. & Jackson, G. Study of the demixing transition in model athermal mixtures of colloids and flexible self-excluding polymers using the thermodynamic perturbation theory of Wertheim. *J. Chem. Phys.* **118**, 8525–8536 (2003).
65. Saeki, S., Kuwahara, N., Konno, S. & Kaneko, M. Upper and lower critical solution temperatures in polystyrene solutions. *Macromolecules* **6**, 246–250 (1973).
66. Joanny, J. F. Critical properties of a system of two molten polymers. *J. Phys. A* **11**, L117–L120 (1978).
67. Majkrzak, C. F. et al. Determination of the effective transverse coherence of the neutron wave packet as employed in reflectivity investigations of condensed-matter structures. I. Measurements. *Phys. Rev. A* **89**, 033851 (2014).
68. Higgins, A. M. et al. The impact of interfacial mixing on Förster transfer at conjugated polymer heterojunctions. *Adv. Funct. Mater.* **19**, 157–163 (2009).
69. Koch, F. P. V. et al. The impact of molecular weight on microstructure and charge transport in semicrystalline polymer semiconductors—poly(3-hexylthiophene), a model study. *Prog. Polym. Sci.* **38**, 1978–1989 (2013).
70. Saerbeck, T. et al. Recent upgrades of the neutron reflectometer D17 at ILL. *J. Appl. Cryst.* **51**, 249–256 (2018).
71. Campbell, R. A. et al. FIGARO: the new horizontal neutron reflectometer at the ILL. *Eur. Phys. J.* **126**, 107 (2011).
72. Gutfreund, P. et al. Towards generalized data reduction on a chopper-based time-of-flight neutron reflectometer. *J. Appl. Cryst.* **51**, 606–615 (2018).
73. Nelson, A. Co-refinement of multiple-contrast neutron/X-ray reflectivity data using motif. *J. Appl. Cryst.* **39**, 273–276 (2006).

Acknowledgements

We thank the ILL and ISIS for the award of beam time (experiment numbers 9–12–387 (Figaro), 9–12–456 (D17) and RB 1620066 (Inter)), and the staff of D17, Figaro and Inter for help during the experiments. We also thank Diamond Light Source for the award of beamtime (S115486–1) and Tom Arnold and Chris Nicklin at beam-line I07 for their support during the GIXD experiments. E.H. acknowledges Swansea University for funding her PhD studentship, and D.M. acknowledges the UK Engineering and Physical Sciences Research Council (EPSRC) for funding his studentship via the Doctoral Training Grant to Swansea University. A.D. acknowledges the EPSRC for funding through the EPSRC Supergen Solar Challenge Grant: EP/M025020/1. We acknowledge Leeds EPSRC Nanoscience and Nanotechnology Facility (LENNF) and Michael B. Ward for providing access to transmission electron microscopy instrumentation and support. We thank Fabrizia Foglia for help with neutron reflectivity measurements on a couple of samples, and Noura Alhazmi, Samuele Lilliu, Edwin Pindea De La O and Fabio Pontecchani for help with the GIXD experiments on beamline I07 at Diamond. A.J.P. thanks Xenocs for their help and ongoing support in the GIXD user program in Sheffield, and

we thank EPSRC for funding the purchase of this instrument. Sebastian Pont is thanked for performing the atomic force microscopy measurements shown in Supplementary Fig. 13.

Author contributions

The overall structure of the project was designed by A.H., with help from E.H. A.H., E.H. and D.M. were responsible for the formulation of hypotheses, the development of sample preparation methodologies and the design of experiments. E.H. performed the sample preparation, with support from A.H. The neutron scattering experiments were performed by E.H., A.H., J.C., P.G. and R.W. GIXD experiments were performed by A.J.P., A.D. and E.H. Transmission electron microscopy was performed by D.M. Data analysis was performed by E.H., with support from A.H. All authors contributed to the writing of the paper.

Additional information

Supplementary information accompanies this paper at <https://doi.org/10.1038/s42005-019-0211-z>.

Competing interests: The authors declare no competing interests.

Reprints and permission information is available online at <http://npg.nature.com/reprintsandpermissions/>

Publisher's note Springer Nature remains neutral with regard to jurisdictional claims in published maps and institutional affiliations.



Open Access This article is licensed under a Creative Commons Attribution 4.0 International License, which permits use, sharing, adaptation, distribution and reproduction in any medium or format, as long as you give appropriate credit to the original author(s) and the source, provide a link to the Creative Commons license, and indicate if changes were made. The images or other third party material in this article are included in the article's Creative Commons license, unless indicated otherwise in a credit line to the material. If material is not included in the article's Creative Commons license and your intended use is not permitted by statutory regulation or exceeds the permitted use, you will need to obtain permission directly from the copyright holder. To view a copy of this license, visit <http://creativecommons.org/licenses/by/4.0/>.

© The Author(s) 2019